

A Phantom Study to Determine the Theoretical Accuracy and Precision of Radial MRI to Measure Cross-Sectional Area Differences for the Application of Coronary Endothelial Function Assessment

Jérôme Yerly,^{1,2} Danilo Gubian,³ Jean-Francois Knebel,^{2,4} Ali Schenk,⁵ Jerome Chaptinel,¹ Giulia Ginami,¹ and Matthias Stuber^{1,2*}

Purpose: MRI has been used to noninvasively assess coronary endothelial function by measuring the vasoreactivity in response to handgrip exercise. However, the spatial resolution of MRI is limited relative to the expected vasodilation response of healthy coronary arteries (10%–20%), and the sensitivity of MRI to detect such small cross-sectional area differences has yet to be quantitatively examined.

Methods: Holes of different diameters were drilled in a phantom to simulate a range of physiological responses of coronary arteries to stress. Radial cine MR images with different spatial resolutions were acquired under moving conditions, and different noise levels were simulated. Cross-sectional areas were automatically measured and statistically analyzed to quantify the smallest detectable area difference.

Results: Statistical analyses suggest that radial MRI is capable of distinguishing area differences of 0.2 to 0.3 mm² for high signal-to-noise ratio images, which correspond to a percentage coronary area difference of 3% to 4% for a 3-mm baseline diameter. Furthermore, the smallest detectable area difference was largely independent of the pixel size for the sequence and range of diameters investigated in this study.

Conclusion: Radial MRI is capable of reliably detecting small differences in cross-sectional areas that are well within the expected physiological range of stress-induced area changes in of healthy coronary arteries. *Magn Reson Med* 79:108–120, 2018. © 2017 International Society for Magnetic Resonance in Medicine.

Key words: Coronary; endothelial function; radial MRI; accuracy; precision; vasoreactivity; vasodilation; limit of detection

INTRODUCTION

The endothelium is a thin monocellular layer that serves multiple functions and plays an important role in many aspects of cardiovascular health. Among those, the endothelium acts as a semi-selective barrier to regulate fluid and molecule traffic between blood and tissue, maintains vascular homeostasis, serves as a nonthrombogenic surface, contributes to angiogenesis and tissue wound-healing, and regulates vascular tone and blood flow (1,2). Impairment of these normal vascular functions, known as *endothelial dysfunction*, most often results from an increased oxidative stress (3,4) and has been linked to pathological inflammatory processes and future adverse cardiovascular events (4–8). Although measuring any of the endothelium's functions may provide information about the integrity and general health of said endothelium, for practical reasons a frequently investigated aspect in clinical research is the regulation of vascular tone in response to endothelial-dependent stressors (9–13).

Assessment of the vasomotor response of the epicardial coronary arteries, using invasive imaging modalities such as coronary angiography (9) and intravascular ultrasound (14), has shown that healthy coronary arteries dilate by about 10% to 25% in response to endothelium-dependent stressors via the release of nitric oxide (15). Conversely, reduced dilation and even paradoxical vasoconstriction are observed in impaired coronary arteries (9). However, because of their invasive nature, these imaging modalities are restricted to patients with advanced disease and are not clinically justifiable for use in screening or longitudinal studies.

To address these limitations, and to noninvasively discriminate normal from abnormal coronary endothelial function, recent studies have proposed using MRI with isometric handgrip exercise (13,16–18) as the endothelial-dependent stressor. This promising new technique has yielded excellent and reproducible results (18). However, the sensitivity of MRI to measure small changes in cross-sectional area of the coronary arteries, in response to stress, has yet to be quantitatively examined. Because the spatial resolution of MRI is limited relative to the expected area changes, it is of utmost importance to address this question.

In this study, we have designed a phantom that simulates a physiological range of coronary cross-sectional areas and used it to measure the sensitivity of MRI for detecting small area differences under both static conditions and mounted

¹Department of Radiology, University Hospital (CHUV) and University of Lausanne (UNIL), Lausanne, Switzerland.

²Center for Biomedical Imaging (CIBM), Lausanne, Switzerland.

³Direction des Constructions, Ingénierie, Technique et Sécurité (CIT-S), University Hospital (CHUV) and University of Lausanne (UNIL), Lausanne, Switzerland.

⁴Laboratory for Investigative Neurophysiology (The LINE), Departments of Radiology and Clinical Neurosciences, University Hospital (CHUV) and University of Lausanne (UNIL), Lausanne, Switzerland.

⁵Quality Management, Liebherr Machines Bulle SA, Bulle, Switzerland.

Grant sponsor: Research funding for this project was provided by the Swiss National Science Foundation grants 320030_143923 and 326030_150828.

*Correspondence to: Matthias Stuber, PhD, University Hospital of Lausanne (CHUV), Rue de Bugnon 46, BH 8-80, 1011 Lausanne, Switzerland. E-mail: mstuber.mri@gmail.com.

Correction added after online publication 21 March 2017. The PDF was reloaded to correct symbols due to a conversion issue. The authors have also resupplied Figures 1, 2, 3, 6, 7, 8 to improve image quality.

Received 25 July 2016; revised 23 January 2017; accepted 24 January 2017

DOI 10.1002/mrm.26646

Published online 5 March 2017 in Wiley Online Library (wileyonlinelibrary.com).

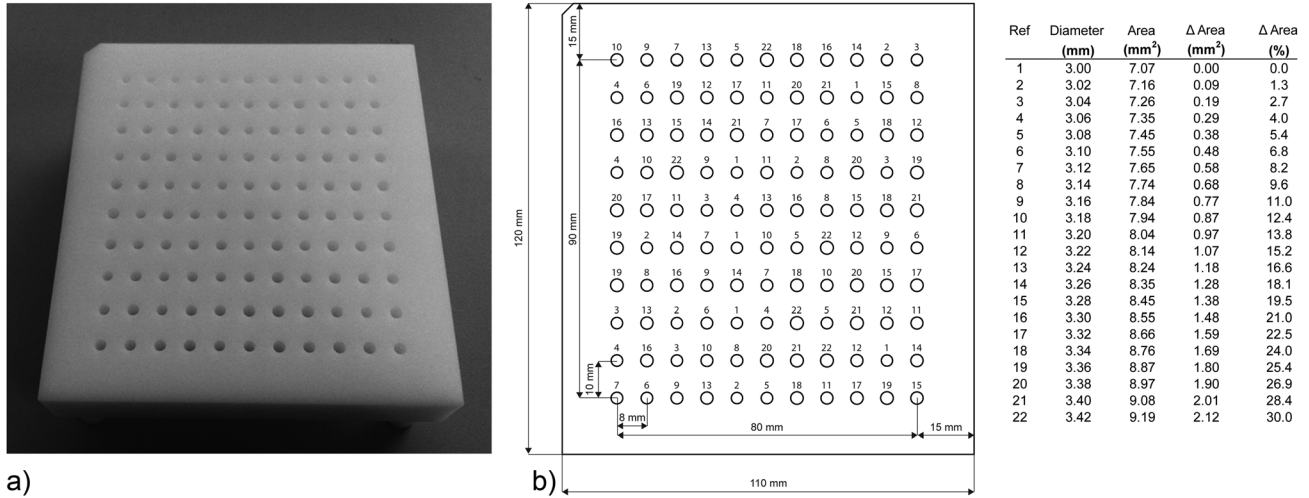


FIG. 1. Design of the coronary mimicking phantom. (a) Picture of the phantom. (b) Drilling layout of the phantom indicating the position and diameter of the drilled holes. The 22 drilled diameters ranged from 3.00 $-0/+0.004$ mm to 3.42 $-0/+0.004$ mm, in steps of 0.02 mm, and were repeated at five different locations on the phantom, adding up to a total of 110 holes.

on a moving MR-compatible platform. Radial cine MR images were acquired with different spatial resolutions and different signal-to-noise ratios (SNRs) were simulated by adding artificial noise to the images. Cross-sectional areas were measured with a fully automated procedure and compared to known nominal values.

METHODS

Moving Phantom Design

A phantom was designed to simulate a range of cross-sectional areas of coronary arteries by drilling holes of different diameters in a block of Polyacetal copolymer (POM-C) (Fig. 1a) using high precision reamers (MAGAFOR, Fontenay-sous-Bois, France). The average lumen diameter of the proximal segment of a normal human coronary artery (left or right system) is about 3.0 to 4.5 mm (19). To account for the lower range of proximal human coronary artery dimensions, holes were drilled with diameters d ranging from 3.00 $-0/+0.004$ mm to 3.42 $-0/+0.004$ mm, in steps of 0.02 mm, creating $N_d = 22$ lumen diameters. This range of diameters also corresponds to a maximal area difference of 30% (Fig. 1b), consistent with the magnitude of physiological response of healthy coronary arteries (9,13,14,16–18). In addition, each hole with a given diameter was drilled at five different locations on the phantom, accounting to a total of 110 holes that are available for analysis. The holes were assigned to random locations to minimize potential bias in the measurements due to magnetic field inhomogeneities (Fig. 1b).

The coronary mimicking phantom was placed in a container filled with tap water and doped with gadolinium (DOTAREM, Guerbet, Roissy, France) to account for the time-of-flight in-flow contrast of 2D cine imaging and to obtain a SNR similar to that of in vivo images. The average in vivo SNR was computed using our previously reported data (20), which were acquired with the same 2D radial retrospectively electrocardiography (ECG)-gated sequence used in the present study. This included a

0.6 mm in-plane resolution (see below for more details). Five in vivo sample datasets were selected, and the average SNR was computed by manually selecting a region of interest in the coronary artery and another one in a region void of signal outside of the chest. The concentration of gadolinium in the phantom was then adjusted to match this in vivo SNR.

The phantom was then placed on a custom, home-built moving phantom similar to the one in (21) to mimic a unidirectional sinusoidal cardiac motion. The setup was programmed to rotate with a frequency of 40 bpm and a maximal displacement of 3 cm. Furthermore, the unit provided a triggering signal to synchronize the MR cine acquisition with the phantom motion.

MR Image Acquisition

The study was performed on a clinical 3.0 T MR scanner (MAGNETOM Prisma, Siemens AG, Healthcare Sector, Erlangen, Germany) with an 18-channel chest coil array and a 32-channel spine coil array for signal reception. A high spatial resolution localizer was first acquired in order to plan the subsequent imaging slice orientation perpendicular to the drilled holes of the mock coronary phantom. MR images of the phantom were then acquired using a conventional vendor-product 2D radial, retrospectively gated, spoiled gradient recalled echo (GRE) cine sequence (20). The images were acquired under both static and moving conditions. The acquisition under moving condition was triggered with the signal provided by the moving phantom setup described above. To investigate the effect of the acquired spatial resolution on the measurement of the cross-sectional areas, five different isotropic in-plane image resolutions (isotropic pixel size $p=0.5, 0.6, 0.7, 0.8$ and 0.9 mm) were studied. For each resolution, the acquisition was repeated 10 times with the parameters given in Table 1. Although the mock coronary phantom did not simulate epicardial fat, a product fast water-selective excitation

Table 1
MRI Acquisition Parameters

| Parameter | Pixel Size | | | | |
|----------------------------|--|-----------|-----------|-----------|-----------|
| | 0.5 mm | 0.6 mm | 0.7 mm | 0.8 mm | 0.9 mm |
| Sequence | 2D radial, retrospectively gated, spoiled GRE cine | | | | |
| Fat sat | Water selective excitation pulse | | | | |
| Radial views | 247 per cardiac phase | | | | |
| Number of R-R intervals | 13 | | | | |
| Views per segment | 19 | | | | |
| RF excitation angle (°) | 22 | | | | |
| Temporal resolution (ms) | 40 | | | | |
| Slice thickness (mm) | 6.5 | | | | |
| Acquisition time (s) | 19.5 | | | | |
| FOV (mm) | 260 × 260 | | | | |
| Image matrix (pixel) | 512 × 512 | 416 × 416 | 384 × 384 | 320 × 320 | 288 × 288 |
| Pixel size (mm) | 0.5 × 0.5 | 0.6 × 0.6 | 0.7 × 0.7 | 0.8 × 0.8 | 0.9 × 0.9 |
| TE/TR (ms) | 2.9/5.1 | 2.7/4.9 | 2.7/4.9 | 2.6/4.9 | 2.5/4.9 |
| Pixel bandwidth (Hz/pixel) | 575 | 570 | 545 | 540 | 510 |
| Radial undersampling (%) | 31 | 38 | 41 | 49 | 55 |

FOV, field of view; GRE, gradient recalled echo; RF, radiofrequency; TE, echo time; TR, repetition time; R-R, time between consecutive QRS complexes or heartbeats.

pulse was nevertheless used as to keep the protocol consistent with previously reported in vivo studies (20).

Gold Standard Diameter Measurements

To verify the accuracy and precision of the phantom manufacturing, the drilled cross-sectional areas were measured using a highly accurate precision machine (Werth VideoCheck HA, Werth Messtechnik GmbH, Gießen, Germany). The drilled diameters were measured with a touch trigger probe, which has length measuring deviations of less than 0.5 μm . Bland-Altman plots and linear regression analyses were used to evaluate the correlation and agreement between the known, drilled cross-sectional areas and the actual gold standard measurements.

Cross-Sectional Area Measurements

On the MR images, the cross-sectional areas of the drilled holes were computed using a fully automated custom-written software package developed in MATLAB (MathWorks, Natick, MA, USA). The algorithm automatically detected and segmented the lumen of the drilled holes. The segmentation, based on the full-width half maximum criterion (FWHM), followed a similar procedure as described previously (20). Figures 2a–e illustrates the various stages of the segmentation. The images were first low-pass filtered with a Gaussian filter and then interpolated onto a $10 \times$ oversampled grid using a bicubic interpolation. Low-pass filtering was implemented in image space as a 2D convolution operator using a 3×3 Gaussian kernel. A fixed $10 \times$ oversampling factor was chosen to be consistent with the approach used in previous studies (13,16–18,22), which used a semiautomated software tool (Cine version 3.15.17, General Electric, Milwaukee, Wisconsin, USA) to measure the cross-sectional area. The bicubic interpolation computed a weighted average of pixels in the nearest 4-by-4 neighborhood. The algorithm then selected an arbitrary point inside the lumen of each drilled hole by finding the pixel with the maximum signal

intensity (Fig. 2b). Originating from this point, a total of 360 uniformly distributed radial profiles were further interpolated from the interpolated image (Fig. 2c) and analyzed to identify the lumen border using the FWHM criterion (Fig. 2d). Linear interpolation was used to precisely determine the FWHM position along the radial profiles (Fig. 2f). The segmentation result, that is, the polygon formed by the set of vertices corresponding to the FWHM position along every radial profile (Fig. 2e), was then used to geometrically compute the cross-sectional area of the lumen. To investigate the reproducibility of the area measurements, the images were processed twice with the algorithm. Bland-Altman plots and linear regression analyses were used to evaluate the correlation and agreement between the repeated measurements.

Given the sinusoidal motion of the moving phantom, there are two positions of minimal velocity from which MR cine frames were visually selected and used for cross-sectional area measurements. Similarly, two frames were also selected and processed from the static phantom acquisitions. Comparing the area measurements between the two frames under both static and moving conditions allowed for characterization of the different sources of measurement variability. For the static experiment, it is reasonable to assume that the variability of measurements mainly originates from unavoidable sources such as thermal noise. For the moving experiment in turn, the area measurements may additionally be affected by residual motion and magnetic field inhomogeneities. Bland-Altman plots and linear regression analyses were used to evaluate the correlation and agreement of the area measurements between the two selected frames. Paired-sample Student *t* tests were used to determine whether the standard deviation (SD) of the differences between the two measurements observed in the static dataset significantly differed from the one under moving conditions.

Noise Simulation

The SNR was computed and recorded for each segmented hole. The SNR in the original images depends on several

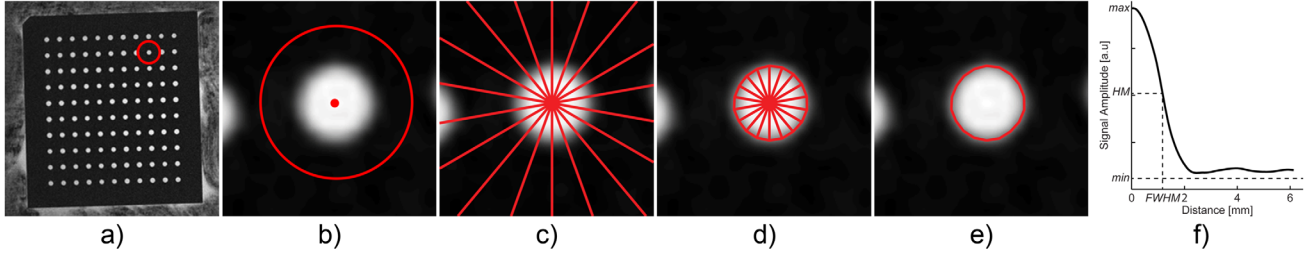


FIG. 2. Overview of the different computational steps of the fully automated custom-written software used to measure the cross-sectional area of the drilled holes. (a) Selected cine frame with minimal visible motion artifacts. (b) An arbitrary point inside the lumen of every drilled hole is automatically selected by finding the pixel with the maximum signal intensity. (c) A total of 360 uniformly distributed cross-sectional profiles were obtained by interpolating the image along radial trajectories originating from the selected point inside the vessel lumen. For clarity, the illustrated example only shows 18 profiles originating from the center. (d) The software analyzed these radial profiles and automatically segmented the vessel lumen using the full-width half maximum criterion (f), yielding a set of vertices $V = \{v_0, v_1, \dots, v_{359}\}$ that delineates the edge of the drilled hole. (e) The vessel lumen area, $A(V)$, was obtained by geometrically computing the polygon area formed by the vertices V . HM = half maximum.

parameters, including the gadolinium concentration; spatial resolution; receiver bandwidth; and number of radial views, which were kept constant. The high concentration of gadolinium used in this study ensured a high SNR of the luminal signal μ_{signal} given by $\text{SNR}_{\text{original}} = \mu_{\text{signal}}/\sigma_{\text{noise}}$, where σ_{noise} is the SD of the noise in the original images, as measured in a region void of signal outside of the chest. To investigate the effect of SNR on the measurement of the cross-sectional areas, images with a lower SNR, which was defined by $\text{SNR}_{\text{new}} = \alpha * \text{SNR}_{\text{original}}$; $\alpha = \{1.00, 0.75, 0.50\}$, were simulated by adding noise to the original images. The three different α values are thereafter referred to as noise level (n) of 0, 1, and 2, respectively.

The SD of the added noise was given by $\sigma_{\text{added}} = \sigma_{\text{noise}} \sqrt{\alpha^{-2} - 1}$. This added noise image was obtained by simulating noise from an $N_c = 16$ element coil for both the real and imaginary components. The SD of the Gaussian noise in the real and imaginary images (which were assumed to be equal) were derived from the chi distribution and were given by $\sigma_{\text{coil}} =$

$$\sigma_{\text{added}} / \sqrt{k - \left(\sqrt{2} \frac{\Gamma((k+1)/2)}{\Gamma(k/2)} \right)^2}, \text{ where } \Gamma \text{ is the gamma}$$

function and $k = 2N_c$ is the number of independent, normally distributed random variables. Each coil image was simulated by replicating the original magnitude image normalized by the square root of the number of coils N_c and by adding the corresponding complex noise. The final image with simulated noise was then obtained by performing a sum-of-squares reconstruction of the coil images.

Accuracy and Precision of Area Measurements

The areas A measured for each drilled diameter d , noise level n , pixel size p , and moving condition m (ie, static or moving) were grouped together for statistical analysis and are denoted by $A_{d,n,p,m}$. The normality of the measurements was tested using both the Lilliefors and Jarque-Bera tests. The expected value or mean $\mu_{A_{d,n,p,m}} = E[A_{d,n,p,m}]$ and variance $\sigma_{A_{d,n,p,m}}^2 = E[(A_{d,n,p,m} - \mu_{A_{d,n,p,m}})^2]$ were computed for each distribution. The accuracy of the measurements was defined as the bias or deviation of the mean from the known drilled area, that is,

$\mu_{A_{d,n,p,m}} - \pi d^2/4$, whereas the precision was determined by the SD $\sigma_{A_{d,n,p,m}}$ (Fig. 3a). Linear regression analyses were also used to evaluate the correlation and agreement between the measured and known drilled cross-sectional areas.

Limit of Detection of Area Difference

A statistical test based on the area under the curve (AUC) of the receiver operating characteristic (ROC) curve (23–26) was used to quantify the sensitivity of radial MRI to detect small differences in cross-sectional areas. Figures 3b–e illustrates an overview of the statistical test. Given two diameters d_i and d_j , a nonparametric ROC curve (which does not make any assumption about the underlying distribution of the data) was computed from the two randomly measured variables (ie, areas) $A_{i,n,p,m}$ and $A_{j,n,p,m}$. The corresponding area under the ROC curve, $\text{AUC}_{i,j,n,p,m}$, was computed and recorded for further analysis. The true change in cross-sectional area between the two diameters, $\Delta_{\text{area},ij} = \pi(|d_i^2 - d_j^2|)/4$, was considered statistically detectable if $\text{AUC}_{i,j,n,p,m} \geq 0.95$ (Figs. 3d–e). Each pair of diameters d_i and d_j was compared using the above test. Next, the smallest area difference that passed this statistical test was determined for every diameter d_j . The smallest detectable area difference with radial MRI or limit of detection (LOD), $\text{LOD}_{n,p,m}$, was then defined as the mean of these smallest detectable area differences. The $\text{LOD}_{n,p,m}$ is thus independent of the hole diameter. The standard error of the smallest detectable area differences was also computed to quantify the variability. Finally, the LOD values were reported as absolute area differences in mm^2 , area difference relative to pixel area in pixels, and area difference relative to a 3-mm nominal diameter in %.

Analysis of Variance

One-way analysis of variance (ANOVA) was used to test whether the pixel size or moving condition had a significant effect on the SNR, accuracy, precision, and LOD of area differences. Post hoc Tukey's tests were performed to further identify the source of the differences when overall significance ($P < 0.05$) was found with ANOVA. This test was only performed on the data from the original images (ie, noise

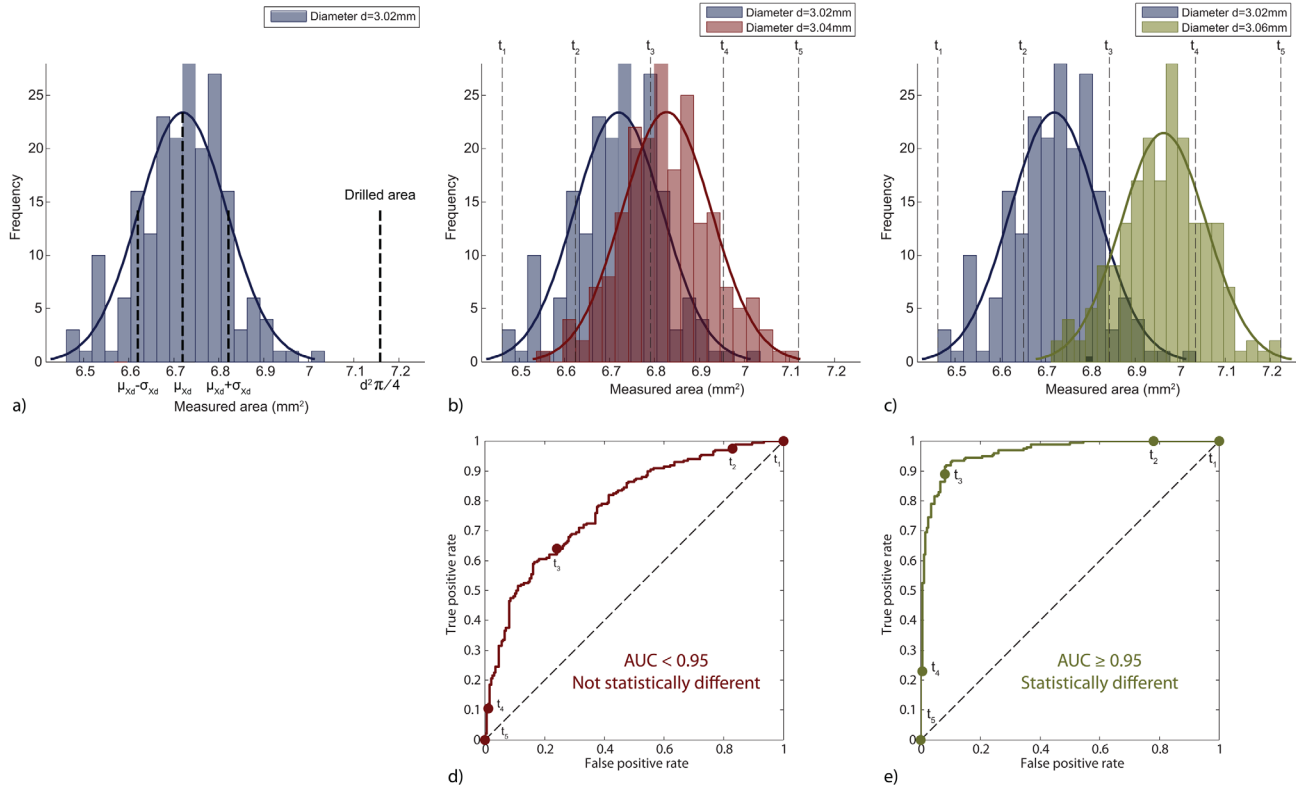


FIG. 3. Illustration of the different statistical analyses used in this study. (a) Frequency plot of the area measurements for a given diameter d modeled by a normal distribution with mean μ_{X_d} and SD σ_{X_d} . The accuracy of the measurements was defined as the bias or deviation of the mean from the known drilled area, that is, $\mu_{X_d} - \pi d^2/4$, whereas the precision was determined by the SD σ_{X_d} . Subfigures (b–e) illustrate an overview of the statistical test based on the AUC of the ROC curve to determine the smallest detectable area difference with radial MRI. The area measurements from two different diameters were considered statistically different if $AUC \geq 0.95$. The ROC curves in (d) and (e) are obtained by evaluating the true and false positive rates at various decision thresholds (t_1 – t_5) on the continuous variable (ie, measured area) of subfigures (b) and (c), respectively. AUC, area under the curve; ROC, receiver operating characteristic; SD, standard deviation.

level 0) because adding artificial random noise does not contribute to any meaningful statistical differences.

RESULTS

Figure 4 illustrates representative images that were acquired with the five different spatial resolutions investigated in this study. These images were selected from the ECG-gated cine datasets by choosing the ones corresponding to the period of minimal motion of the moving phantom. An enlarged view of the smallest simulated coronary artery, that is, $d = 3.00\text{ mm}$, is shown in Figures 4f–j using bicubic interpolation. One can observe the gradually increasing blurriness of the lumen border with the larger pixel size. To better illustrate the size of the lumen diameter relative to the spatial resolution of MRI, enlarged views using nearest-neighbor interpolation are also provided in Figures 4k–o.

The average in vivo SNR computed from the five cine datasets acquired in healthy volunteers was 47.9 ± 6.8 . To achieve a similar SNR in the phantom images with 0.6-mm pixel size, the phantom was immersed in a solution doped with gadolinium at a concentration of 5.9 mM. This concentration yielded an SNR of 48.3 ± 3.3 for the phantom when measured under moving condition at the 0.6 mm spatial resolution.

Representative phantom images for the different noise levels and an in vivo image from a healthy volunteer with the same 0.6-mm spatial resolution are illustrated in Figure 5. Note that the suppression of the signal from the epicardial fat surrounding the in vivo coronary artery was imperfect. The remaining epicardial fat signal reduced the apparent conspicuity of the coronary artery and led to a lower contrast-to-noise ratio with the surrounding tissue, relative to the phantom images. However, the SNR of the in vivo image (45.6) was similar to that of the phantom image with noise level 0.

Accuracy and Precision of Cross-Sectional Area Measurements

The drilling of the phantom holes proved to be both highly accurate and precise, as illustrated by the regression analysis (Fig. 6a) and Bland-Altman (Fig. 6b) plots. The gold standard area measurements with the Werth precision machine yielded a SD of 0.033 mm^2 and a nonsignificant bias of 0.005 mm^2 .

Repeated measurements of the cross-sectional areas with the FWHM algorithm, that is, applying twice the algorithm on the same MR images, resulted in identical values, where the slope and intercept of the regression analyses were exactly 1 and 0, within machine precision (Figs. 6c–d).

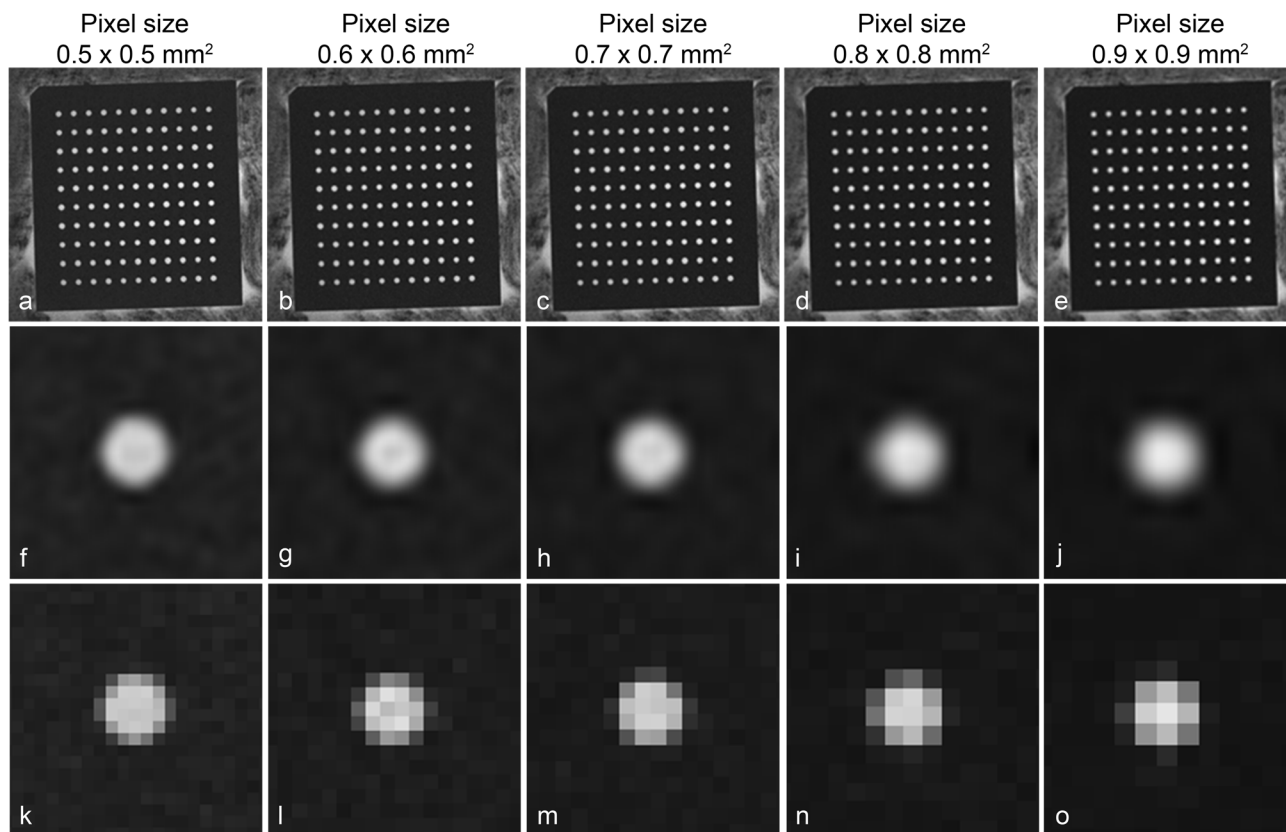


FIG. 4. Representative images acquired with the five different spatial resolutions investigated in this study: (a–e) full field of view images, (f–j) enlarged views of the smallest simulated coronary artery, $d = 3.00$ mm, with bicubic interpolation, and (k–o) same enlarged views but with nearest-neighbor interpolation.

Figures 6e–f show the variability of the area measurements obtained from two different cine frames under static condition for an image resolution of 0.7 mm. Similarly, Figures 6g–h show the area measurement variability obtained under moving condition for identical image resolution. By visually comparing Figures 6e–f and Figures 6g–h, one can observe the increase in variability/spread of the measurements when under moving condition. The paired-sample Student t test confirmed that the SD of the differences of the two area measurements increased if motion was involved (static = 0.085 ± 0.012 mm²; moving = 0.125 ± 0.007 mm²; $P < 0.001$).

Supporting Figure S1 plots the cross-sectional areas measured with radial MRI under moving condition in function of the known drilled areas for each investigated spatial resolution (rows) and noise level (columns). The linear regressions showed strong agreement between measured and drilled cross-sectional areas, with the slopes of the regression analyses ranging from 0.99 to 1.10 and a high correlation of $r^2 > 0.9$. Visual inspection of the plots indicates that lower SNR images (ie, higher noise level) resulted in a larger spread (ie, lower precision) of the area measurements than with higher SNR data. However, the spatial resolution did not have a visible effect on the spread of the measurements. Unlike for the precision of the area measurements, both the spatial resolution and noise level affected the bias (ie, accuracy) of the measurements. These observations are further confirmed with the accuracy and precision plots shown in Supporting Figures

S2c–f. The slopes of the linear regression analyses for the accuracy (Supporting Figs. S2c–d) and precision (Supporting Figs. S2e–f) ranged from -1.6 to -1.4 and 0.01 to 0.14 , respectively. These results indicate an effect of the spatial resolution on the accuracy, whereas precision remains largely unaffected. The intercepts of the regression analyses revealed an evident effect of the noise level on both the accuracy and precision of measurements.

Additionally, the Lilliefors and Jarque–Bera normality tests confirmed that 84.1% and 87.2% of the distributions, respectively, could be well-modeled by a normal distribution.

SNR Measurements

The SNR values for the different spatial resolutions and simulated noise levels are graphically presented for both the static and moving conditions in Supporting Figure S2a and Supporting Figure S2b, respectively. The same concentration of gadolinium was used for all imaging resolutions and resulted in different SNR levels as a function of the image spatial resolution. As expected, larger pixel sizes yielded a better SNR. When linear regression was performed to quantify this relationship, the slopes of regressions ranged from 23.6 to 43.6 (see Supporting Figures S2a–b).

Limit of Detection of Area Difference

The smallest cross-sectional area difference detectable with radial MRI, $LOD_{n,p,m}$, for every spatial

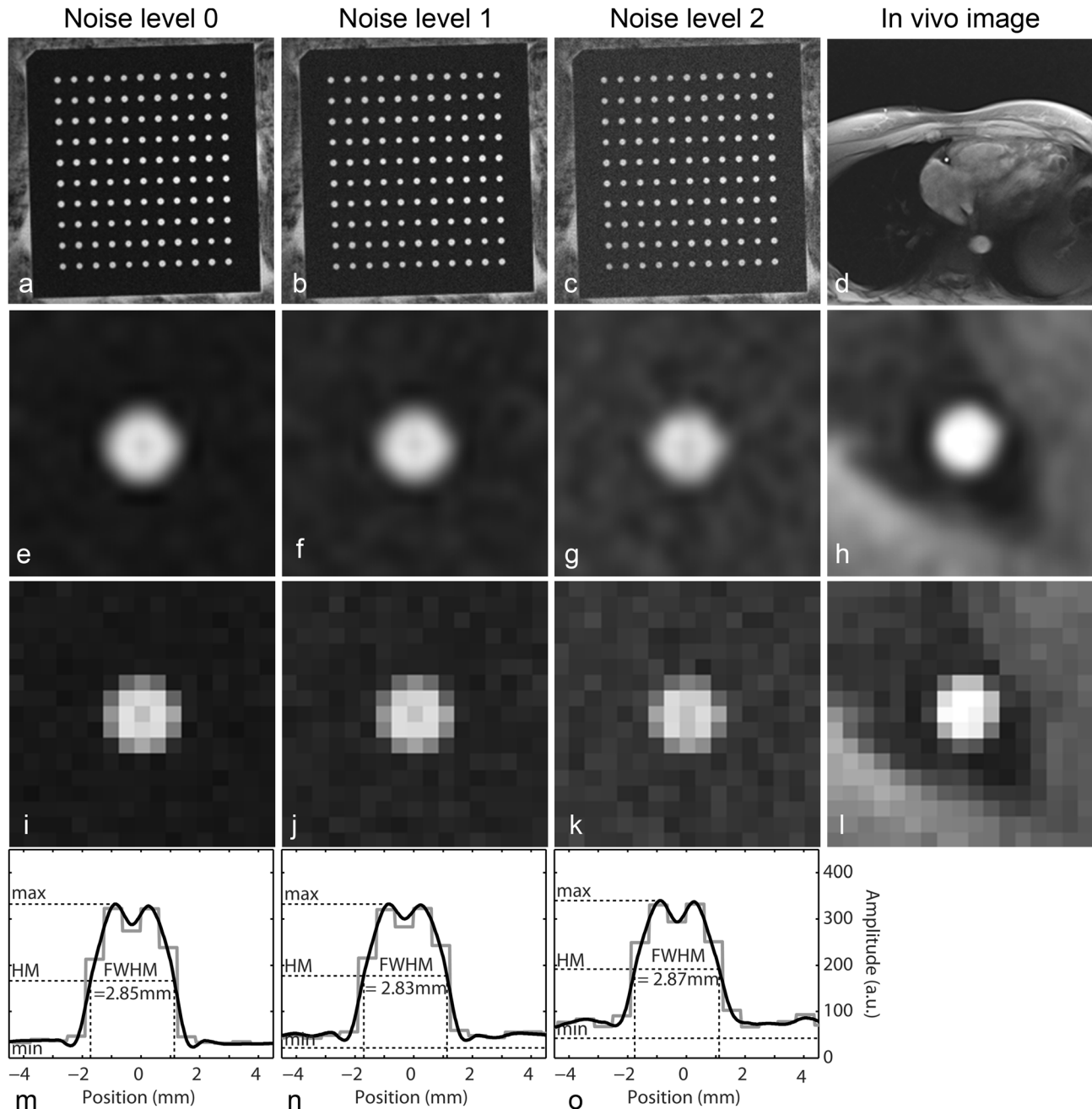


FIG. 5. Representative images acquired with a spatial resolution of 0.6 mm of the phantom for the different noise levels and an in vivo image from a healthy volunteer: (a–d) full field of view images; (e–h) enlarged views of the smallest drilled hole, $d = 3.00$ mm, and the in vivo coronary artery with bicubic interpolation; and (i–l) same enlarged views but with nearest-neighbor interpolation. Line profiles through the center of (e–h) and (i–l) are provided in (m–o). FWHM, full width half maximum criterion.

resolution and noise level is illustrated in Figure 7a for the static phantom and in Figure 7b for the moving one. Visual inspection of the graphs established that the pixel size had very little impact on LOD, which was confirmed with the linear regressions. The slopes of regression were close to zero and ranged from 0.07 to 0.14 and 0.04 to 0.16 for the static and moving phantom, respectively. In contrast, the smallest detectable area difference was highly dependent on the noise level. For the static phantom, the average LOD ranged from 0.20 to 0.26 mm² (2.83%–3.68%); 0.26 to 0.32 mm² (3.68%–4.57%); and

0.41 to 0.46 mm² (5.81%–6.49%) for the noise level 0, 1, and 2, respectively. The moving phantom yielded similar ranges of values, that is, 0.21 to 0.26 mm² (2.97%–3.68%); 0.27 to 0.34 mm² (3.88%–4.84%); and 0.45 to 0.51 mm² (6.39%–7.25%) for the noise level 0, 1, and 2, respectively.

Table 2 shows the same LOD data as in Figures 7a–b, but in different formats, including the absolute area difference in mm², area difference relative to pixel area in pixels, and area difference relative to a 3-mm nominal diameter in %.

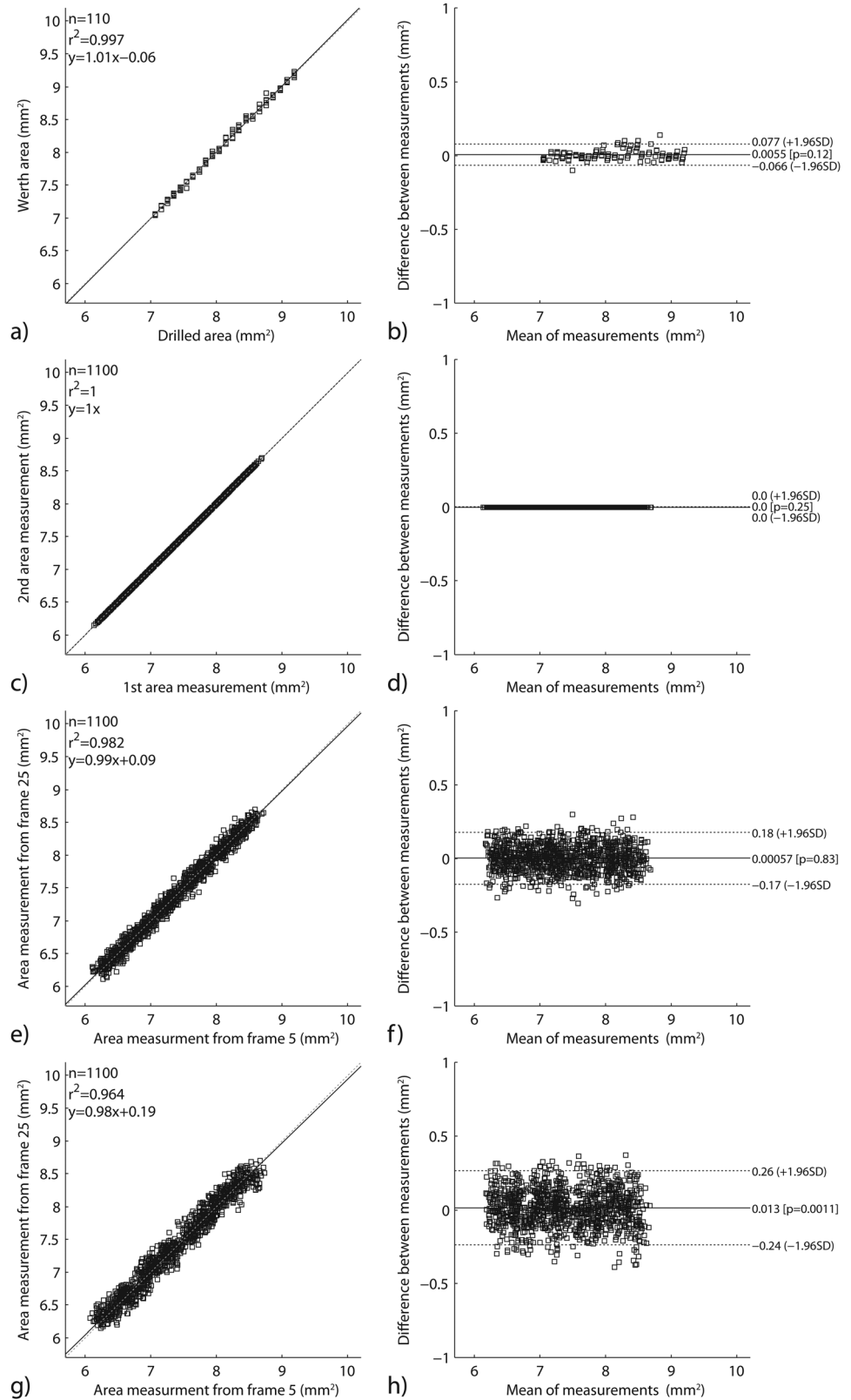


FIG. 6. Linear regression analyses (left column) and Bland-Altman plots (right column) of various comparisons of area measurements. (a–b) Comparison of the gold standard area measurements using the Werth precision machine versus the known drilled area. (c–d) Comparison of repeated area measurements with the full-width half maximum criterion algorithm applied twice on the same images. (e–f) Comparison of the area measurements from two different cine frames from the static phantom. (g–h) Comparison of the area measurements from two different cine frames from the moving phantom (ie, at different physical positions of the phantom).

Analysis of Variance

Supporting Figure S3 illustrates the summary of the ANOVA and post hoc analyses that were performed on the SNR, accuracy, and precision results, whereas Figure

8 shows the analyses that were performed on the LOD results.

One-way ANOVA showed that both the moving condition and spatial resolution had a statistically significant effect on the SNR results. The SNR values measured under

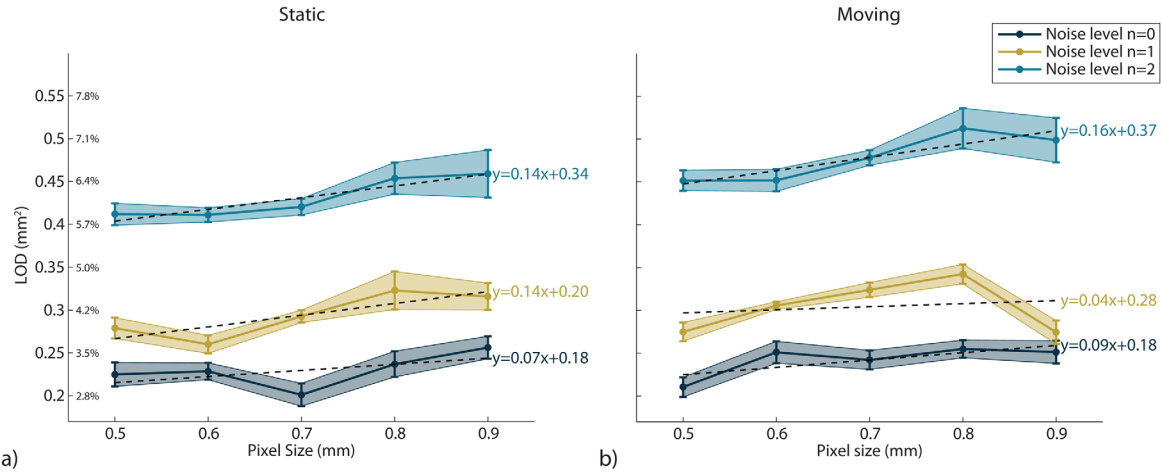


FIG. 7. Plots of the results for the LOD or smallest detectable area difference under static (a) and moving (b) conditions. Subfigures show the mean and standard error of the LOD for every n, p , and m . For the reader's convenience, the LOD axis (vertical axis) is provided in absolute area differences in mm^2 (outer scale) and area difference relative to a 3-mm nominal diameter in % (inner scale). LOD, limit of detection.

moving condition were significantly lower than the static SNR values (static = 54.30 ± 6.67 ; moving = 53.00 ± 6.02 ; $F(1,210) = 40.05$; $P < 0.001$), as shown in Supporting Figure S3a. The means of the SNR values for the different spatial resolutions in Supporting Figure S3b were also all significantly different from one another ($F(4,210) = 890.97$; $P < 0.001$).

The accuracy results attained statistical significance for all of the spatial resolutions ($F(4,210) = 760.04$; $P < 0.001$) (Supporting Fig. S3d), but none between the static and moving measurements ($F(1,210) = 0.00$; $P = 0.98$) (Supporting Fig. S3c).

Regarding the precision results, there was a statistically significant difference between spatial resolution groups, as determined by one-way ANOVA ($F(4,210) =$

2.76 ; $P = 0.029$). The post hoc Tukey test indicated that the statistically significant difference was between pixel sizes of 0.7 mm and 0.9 mm (Supporting Fig. S3f). The area measurements under static condition were on average $0.005 \pm 0.021 \text{ mm}^2$ more precise than the moving measures (Supporting Fig. S3e), but statistical significance was not reached ($F(1,210) = 2.38$; $P = 0.124$).

One-way ANOVA of the LOD results indicated a statistically significant difference between spatial resolution groups ($F(4,210) = 3.12$; $P = 0.016$). The post hoc Tukey test revealed that the statistically significant difference was between pixel size groups of 0.5 mm and 0.9 mm (Fig. 8b). No statistically significant difference was observed between the static and moving data (Fig. 8a). The LOD results under moving condition were on

Table 2

LOD for Static and Moving Phantom^a Reported as Absolute Area Difference in mm^2 , Area Difference Relative to Pixel Area in Pixels, and Area Difference Relative to 3-mm Nominal Diameter in %

| Pixel Size | Noise Level | | |
|------------|--|-------------------------------|-------------------------------|
| | 0 | 1 | 2 |
| | Area Change in (mm^2) | | |
| 0.5 mm | $0.22 \pm 0.01/0.21 \pm 0.01$ | $0.28 \pm 0.01/0.28 \pm 0.01$ | $0.41 \pm 0.01/0.45 \pm 0.01$ |
| 0.6 mm | $0.23 \pm 0.01/0.25 \pm 0.01$ | $0.26 \pm 0.01/0.31 \pm 0.00$ | $0.41 \pm 0.01/0.45 \pm 0.01$ |
| 0.7 mm | $0.20 \pm 0.01/0.24 \pm 0.01$ | $0.29 \pm 0.01/0.32 \pm 0.01$ | $0.42 \pm 0.01/0.48 \pm 0.01$ |
| 0.8 mm | $0.24 \pm 0.01/0.26 \pm 0.01$ | $0.32 \pm 0.02/0.34 \pm 0.01$ | $0.45 \pm 0.02/0.51 \pm 0.02$ |
| 0.9 mm | $0.26 \pm 0.01/0.25 \pm 0.01$ | $0.32 \pm 0.02/0.27 \pm 0.01$ | $0.46 \pm 0.03/0.50 \pm 0.03$ |
| | Area Change Relative to Pixel Area (pixel) | | |
| 0.5 mm | $0.90 \pm 0.06/0.84 \pm 0.05$ | $1.12 \pm 0.05/1.10 \pm 0.04$ | $1.65 \pm 0.05/1.81 \pm 0.05$ |
| 0.6 mm | $0.63 \pm 0.03/0.70 \pm 0.04$ | $0.72 \pm 0.03/0.85 \pm 0.01$ | $1.14 \pm 0.02/1.26 \pm 0.04$ |
| 0.7 mm | $0.41 \pm 0.03/0.49 \pm 0.02$ | $0.60 \pm 0.01/0.66 \pm 0.02$ | $0.86 \pm 0.02/0.98 \pm 0.02$ |
| 0.8 mm | $0.37 \pm 0.02/0.40 \pm 0.02$ | $0.50 \pm 0.03/0.54 \pm 0.02$ | $0.71 \pm 0.03/0.80 \pm 0.04$ |
| 0.9 mm | $0.32 \pm 0.02/0.31 \pm 0.02$ | $0.39 \pm 0.02/0.34 \pm 0.02$ | $0.57 \pm 0.03/0.62 \pm 0.03$ |
| | Area Change Relative to 3 mm Nominal Diameter in (%) | | |
| 0.5 mm | $3.18 \pm 0.20/2.98 \pm 0.16$ | $3.95 \pm 0.17/3.89 \pm 0.16$ | $5.83 \pm 0.18/6.39 \pm 0.17$ |
| 0.6 mm | $3.23 \pm 0.14/3.55 \pm 0.18$ | $3.68 \pm 0.15/4.32 \pm 0.06$ | $5.81 \pm 0.12/6.39 \pm 0.18$ |
| 0.7 mm | $2.84 \pm 0.19/3.43 \pm 0.16$ | $4.14 \pm 0.10/4.58 \pm 0.12$ | $5.95 \pm 0.14/6.77 \pm 0.12$ |
| 0.8 mm | $3.35 \pm 0.21/3.61 \pm 0.15$ | $4.57 \pm 0.31/4.85 \pm 0.16$ | $6.42 \pm 0.26/7.25 \pm 0.33$ |
| 0.9 mm | $3.63 \pm 0.19/3.56 \pm 0.19$ | $4.47 \pm 0.22/3.88 \pm 0.19$ | $6.49 \pm 0.39/7.06 \pm 0.37$ |

LOD, limit of detection.

^aAverage LOD \pm standard error of static data/average LOD \pm standard error of moving data.

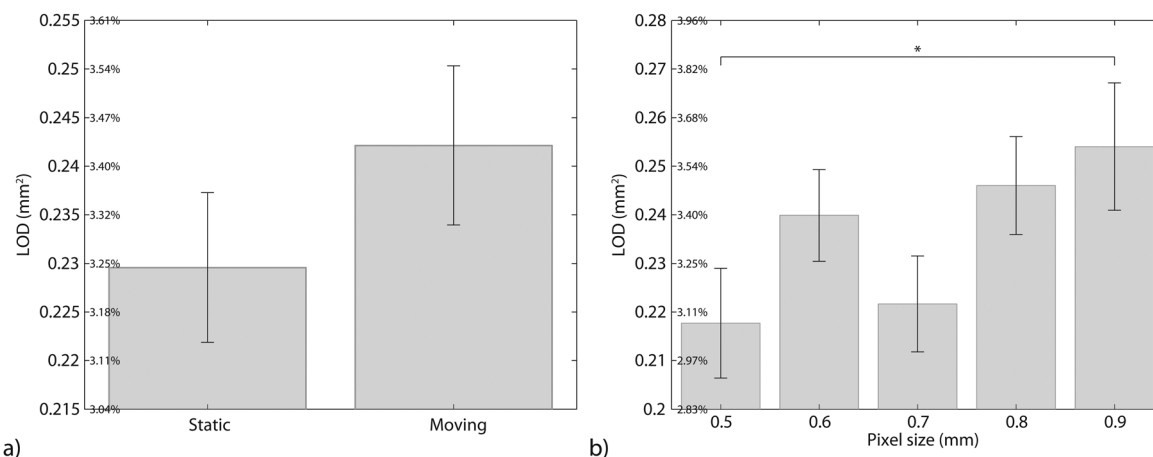


FIG. 8. Bar plots showing the results of the analyses of variance for the LOD results. The graphs illustrate the means and standard errors. Panel (a) compares the means between the static and moving conditions. Panel (b) compares the means between the five different spatial resolutions. The LOD values are provided in absolute area differences in mm² (outer scale) and area difference relative to a 3-mm nominal diameter in % (inner scale). * $P < 0.05$. LOD, limit of detection.

average 0.013 ± 0.061 mm² larger than the static results (ie, lower sensitivity in detecting area differences), but were not statistically significantly different ($F(1,210) = 2.51$) ($P = 0.115$), as illustrated in Figure 8a.

DISCUSSION

In this experimental study with well-controlled boundary conditions, we have investigated the ability of MRI to measure differences in cross-sectional areas in a range that is consistent with physiological responses of the proximal coronary arteries to endothelium-dependent stress. The phantom setup was designed to quantify the accuracy and precision of radial MRI in assessing endothelial function by measuring the smallest cross-sectional area differences that could reliably be detected with high confidence. Radial cine MR images with different spatial resolutions were acquired under static and mock cardiac motion conditions, and different SNRs were simulated by adding artificial noise to the images. Cross-sectional areas were then measured with a fully automated procedure and compared to known nominal values. Statistical analysis suggests that radial MRI is capable of distinguishing area differences in the order of 0.2 to 0.3 mm² for images with high SNR (~ 50), which correspond to a percentage coronary area difference of 3% to 4% for a 3-mm baseline diameter. For low SNR (~ 25 –30) images, radial MRI was able to reliably detect area differences of 0.4 to 0.5 mm² (6%–8%). These results suggest that radial MRI with sufficiently high SNR is clearly adequate for measuring area differences in the range of previously reported endothelium-dependent vasomotor response of the proximal coronary arteries in healthy adult subjects (10%–25%) (9,13,14,16–18). Furthermore, our results indicated that the smallest detectable area difference with radial MRI was largely independent of pixel size in the resolution range that we have investigated. Although well-supported by the results presented in this study, this counterintuitive result warrants further discussion.

One would expect that higher spatial resolution images should result in higher accuracy, precision, and sensitivity in detecting small cross-sectional area differences. It is important to note that lower spatial resolution is associated with a higher SNR simply due to the larger pixel size. Consequently, the positive effect of having an improved SNR may be counterbalanced by a detrimental effect associated with lower spatial resolution. From the data presented in this study, it is unclear whether this is the case; further investigations are necessary to address this question in more detail. Moreover, the number of radial views per cardiac phase was kept constant for every investigated spatial resolution. This was necessary to maintain the acquisition time constant for every experiment and within acceptable breath hold duration. However, increasing the spatial resolution while keeping the number of radial views constant resulted in a higher undersampling of k-space (Table 1). Consequently, the higher spatial resolution images were more prone to undersampling streaking artifacts, which may further hinder the detection of small cross-sectional area differences.

Conversely, the accuracy of the measurements, which was defined as the bias between the measurements and the known drilled areas, was linearly dependent on the spatial resolution (Supporting Figs. S2c–d). This behavior can be explained by visually inspecting the enlarged views in Figures 4f–j. Reduced spatial resolution increased the degree of blurring at the lumen border. As a consequence, the full width at half-maximum segmentation tends to further underestimate the true position of the border. However, only the relative change in cross-sectional area is of interest when assessing coronary endothelial function. The sensitivity of detecting such small differences is essentially defined by precision of the area measurements. Therefore, the precision of the area measurements and the sensitivity in detecting small area differences are closely linked. The results also showed that the area measurements were well-modeled by a normal distribution. Consequently, a lower precision, which corresponds to a larger SD of the

measurements, increases the overlap of the distributions from two different diameters, and in turn results in lower AUC value.

The SD of the area measurements originates from multiple sources, including the phantom manufacturing process, MR image acquisition, and image processing. The careful manufacturing process ensured highly accurate and precise dimensions of the holes, as illustrated in Figures 6a–b. The variation of the drilled diameters introduced by the manufacturing process only accounts for about 30% (0.033 mm^2) of the total SD observed in the measurements of the images for noise level 0, which amounts to $0.097 \pm 0.025 \text{ mm}^2$ and $0.101 \pm 0.019 \text{ mm}^2$ for the static and moving data, respectively. The image processing stage, which includes filtering, interpolation, detection, segmentation, and computation of the cross-sectional areas, was fully automatized in order to remove any potential bias from user input. The repeated processing of the images using this fully automatic procedure demonstrated perfect reproducibility of the measurements (Figs. 6c–d). However, the type of filter, the interpolation factor, the selected point inside the lumen, and the number of radial profiles can also account for some of the variability observed in the measurements. Nevertheless, it is reasonable to assume that the bulk of the measurement variability originates from the MR image acquisition procedure. More specifically, sources such as thermal noise, residual motion, and magnetic field inhomogeneities may contribute to the major part of the measurement SD. Simulation with an analytical phantom would be helpful to further characterize the origins of variability in the measurements.

Our results suggest that partial volume effects in the application of measuring cross-sectional areas of coronary arteries appears to contribute to the precision of a given measurement. The smallest area differences detectable with radial MRI, provided in terms of relative pixel size in Table 2, indicate that radial MRI is capable of reliably detecting area differences significantly smaller than the actual pixel area. A potential explanation for this remarkable result is that the partial volume effect causes blurring of the lumen edges, but that the FWHM maximum segmentation algorithm combined with image interpolation and the intrinsic shape of a coronary artery enables the detection of relative differences in cross-sectional area smaller than the pixel size. A different method to determine the vessel cross-sectional area by thresholding in Radon space was previously reported for microscope images (27). However, the computed area is quantized in steps of multiple integers of pixels; consequently, it would not allow for subpixel precision in calculations of cross-sectional area.

Note that it may be possible for a well-constructed imaging sequence to outperform the results shown here. The study described above was highly conservative in terms of its design parameters. Specifically, the nominal coronary diameter simulated was 3 mm, which is on the lower end of the range of proximal human coronary artery dimensions (28). As such, studies in larger coronaries may be able to detect even smaller % changes in vessel area. Likewise, the radial acquisition used a very high number of radial views per segment (19

views), which corresponds to an acquisition window of 95 ms. This almost certainly increased the contribution of motion, as described in the Limitations section below. In an actual clinical setting, reducing the number of views to fit a given quiescent phase of the cardiac cycle might therefore further minimize the contribution of motion. However, this comes at the expense of SNR or breath-hold duration.

This study focused on characterizing the ability of radial MRI to measure differences in cross-sectional areas. However, some previous studies (13,16–18,29) have relied on spiral trajectories to assess the endothelial response. Although the radial trajectory offers several advantages over the spiral one, including readout oversampling and lower sensitivity to off-resonance effects caused by B_0 inhomogeneity and concomitant gradient fields, a comparative study would prove very valuable and instructive. However, such a comparison is beyond the scope of this study.

Limitations

Traditionally, high spatial and temporal resolution cine MR images are considered paramount to successfully measuring the cross-sectional area of coronary arteries. Such images are collected using segmented techniques acquired over multiple cardiac cycles. However, the repositioning of the coronary arteries from beat to beat is not always exact. The repositioning precision has previously been shown to be $< 1 \text{ mm}$ (30). In addition, area measurements are performed on cine frames corresponding to periods of minimal cardiac motion, but residual motion may still occur during data acquisition. Both the repositioning imprecision of the coronary arteries and residual cardiac motion are expected to further decrease the sensitivity of MRI in detecting small area differences of the coronary arteries.

Although our study did not directly investigate the issue associated with the repositioning of the coronary arteries, it showed that radial MRI was very robust to motion. The amount of displacement experienced by the phantom during a segment acquisition can be analytically determined. Specifically, given the number of views per segment $N_{\text{views}} = 19$, the echo spacing $TR = 5 \text{ ms}$, and the time-dependent position of the moving phantom $x(t) = A \sin(\omega t)$, where $A = 1.5 \text{ cm}$, $\omega = 2\pi/T$, and $T = 1.5 \text{ s}$ (40 bpm), one can compute the displacement occurring during the acquisition of a k-space segment, which will lead to blurring in the reconstructed cine frames. If we assume that the selected cine frame to analyze coincided with the extreme positions of the phantom, then the maximum displacement in our phantom study occurred when the acquisition of the segment started or ended exactly at the maximum of the sine wave at time $t' = T/4$, and is given by $\Delta_x = |x(t' \pm T_s) - x(t')| = A |\sin(\omega(t' \pm T_s)) - \sin(\omega t')| = 0.12 \text{ cm}$, where $T_s = N_{\text{views}} \cdot TR$ is the duration of the k-space segment acquisition. Although this represents the most unfavorable situation, it illustrates the potential displacement experienced by the moving phantom, which is superior to the repositioning precision of the coronary arteries and is still significantly larger than the pixel sizes investigated in this study. Despite this relatively large

displacement, radial MRI was very robust to motion because there were no statically significant differences in terms of accuracy, precision, and smallest detectable area difference between the static and moving data (Fig. 8 and Supporting Fig. S3). The perpendicularity of the radial projections with respect to the direction of motion may be another confounder that may affect the blur introduced into the reconstructed image.

The design of our phantom simulated ideal in vivo coronary imaging experiments by assuming perfectly suppressed signal from the pericardial fat surrounding the coronary arteries. However, residual field inhomogeneities and off-resonance, among other things, can lead to imperfect fat suppression, which then can impede the artery conspicuity and corrupt the segmentation of the vessel lumen.

The heart rate simulated in this study was lower than heart rates usually found in patients and volunteers. However, the simulated sinusoidal cardiac motion was continuously moving and did not exhibit a quiescent phase like in late diastole of real cardiac cycles. Consequently, a lower heart rate was chosen to reduce the residual motion during the acquisition of data segment, and therefore to better emulate acquisitions of late diastolic cardiac phases.

The study investigated five spatial resolutions ranging from 0.5 mm to 0.9 mm to determine the sensitivity of MRI in detecting small area differences. The results indicate that this range of spatial resolutions had negligible impact on the difference in area that could be detected with radial MRI. However, it is likely that an effect of the pixel size would be observed for a broader range of spatial resolutions.

Low-pass filtering the images with a 3×3 Gaussian kernel prior to processing the data is equivalent to apodizing the data in k -space and to removing some of the effects of changing spatial resolution in the data acquisition. This may partly explain why our LOD results may not be strongly dependent on the spatial resolution. However, an in-depth investigation of this effect is beyond the scope of this study.

It should also be noted that the rigid sinusoidal translation used in this study to simulate cardiac motion may not be sufficiently representative of in vivo coronary motion. Simulation of a nonrigid motion with a through plane component may be more adequate. Further, to partially account for in vivo time-of-flight effects, we have added gadolinium to the static water surrounding the phantom. However, such static water condition yields uniform signal intensity across the diameter of the drilled holes. Therefore, it does not adequately simulate the nonuniform signal intensity arising from variable wash-in rates of fresh blood signal across vessel diameters, as would be the case in vivo. This variation in signal intensity across the width of the vessel may also affect the cross-sectional area measurements. In addition, this study did not take into account the potential change in blood flow between the two cine acquisitions that would be performed at rest and during handgrip stress. Additionally, the coronary arteries are never perfectly straight, and their obliquity and tortuosity will also affect the area measurement.

In this study, the SNR was measured as the ratio of the average signal of the lumen over the SD of the noise in a region void of signal outside of the chest or phantom. However, this conventional approach to determine SNR may not be fully adequate for multichannel reconstructions (31,32). Furthermore, the effect of spatial resolution on SNR is weaker than one would expect if only considering the voxel volume and effective sampling time. From the data presented in this study, it is unclear whether this is because the noise is dominated by under-sampling artifact or other aspects of the reconstruction and postprocessing.

CONCLUSION

This work presents a phantom study to validate the use of radial MRI for the assessment of coronary endothelial function. The results presented in this study effectively support that radial MRI is capable of reliably detecting small cross-sectional area differences that are well within the range of physiological coronary area changes in response to an endothelium-dependent stressor. Combined with isometric handgrip exercise, this noninvasive, safe, and quantitative imaging modality may also be used in longitudinal studies in which atherosclerosis progression or the response to therapy is measured as an endpoint.

ACKNOWLEDGMENT

The authors would like to thank Liebherr Machines Bulle SA (Bulle, Switzerland) for providing access to their highly accurate precision machine for the gold standard area measurements, and Bastien Milani for insightful discussions.

REFERENCES

- Galley HF, Webster NR. Physiology of the endothelium. *Br J Anaesth* 2004;93:105–113.
- Esper RJ, Nordaby RA, Vilarino JO, Paragano A, Cacharron JL, Machado RA. Endothelial dysfunction: a comprehensive appraisal. *Cardiovasc Diabetol* 2006;5:4.
- Deanfield J, Donald A, Ferri C; Working Group on E, Endothelial Factors of the European Society of Hypertension, et al. Endothelial function and dysfunction. Part I: Methodological issues for assessment in the different vascular beds: a statement by the Working Group on Endothelin and Endothelial Factors of the European Society of Hypertension. *J Hypertens* 2005;23:7–17.
- Deanfield JE, Halcox JP, Rabelink TJ. Endothelial function and dysfunction: testing and clinical relevance. *Circulation* 2007;115:1285–1295.
- Schachinger V, Britten MB, Zeiher AM. Prognostic impact of coronary vasodilator dysfunction on adverse long-term outcome of coronary heart disease. *Circulation* 2000;101:1899–1906.
- Halcox JP, Schenke WH, Zalos G, Mincemoyer R, Prasad A, Waclawiw MA, Nour KR, Quyyumi AA. Prognostic value of coronary vascular endothelial dysfunction. *Circulation* 2002;106:653–658.
- Schindler TH, Hornig B, Buser PT, Olschewski M, Magosaki N, Pfisterer M, Nitzsche EU, Solzbach U, Just H. Prognostic value of abnormal vasoreactivity of epicardial coronary arteries to sympathetic stimulation in patients with normal coronary angiograms. *Arterioscler Thromb Vasc Biol* 2003;23:495–501.
- Widmer RJ, Lerman A. Endothelial dysfunction and cardiovascular disease. *Glob Cardiol Sci Prac* 2014;2014:291–308.
- Ludmer PL, Selwyn AP, Shook TL, Wayne RR, Mudge GH, Alexander RW, Ganz P. Paradoxical vasoconstriction induced by acetylcholine in atherosclerotic coronary arteries. *N Engl J Med* 1986;315:1046–1051.

10. Cox DA, Vita JA, Treasure CB, Fish RD, Alexander RW, Ganz P, Selwyn AP. Atherosclerosis impairs flow-mediated dilation of coronary arteries in humans. *Circulation* 1989;80:458–465.
11. Hashimoto M, Akishita M, Eto M, Ishikawa M, Kozaki K, Toba K, Sagara Y, Taketani Y, Orimo H, Ouchi Y. Modulation of endothelium-dependent flow-mediated dilatation of the brachial artery by sex and menstrual cycle. *Circulation* 1995;92:3431–3435.
12. Nabel EG, Ganz P, Gordon JB, Alexander RW, Selwyn AP. Dilation of normal and constriction of atherosclerotic coronary arteries caused by the cold pressor test. *Circulation* 1988;77:43–52.
13. Hays AG, Hirsch GA, Kelle S, Gerstenblith G, Weiss RG, Stuber M. Noninvasive visualization of coronary artery endothelial function in healthy subjects and in patients with coronary artery disease. *J Am Coll Cardiol* 2010;56:1657–1665.
14. Puri R, Liew GY, Nicholls SJ, et al. Coronary beta2-adrenoreceptors mediate endothelium-dependent vasoreactivity in humans: novel insights from an in vivo intravascular ultrasound study. *Eur Heart J* 2012;33:495–504.
15. Furchgott RF, Zawadzki JV. The obligatory role of endothelial cells in the relaxation of arterial smooth muscle by acetylcholine. *Nature* 1980;288:373–376.
16. Hays AG, Kelle S, Hirsch GA, Soleimanifard S, Yu J, Agarwal HK, Gerstenblith G, Schar M, Stuber M, Weiss RG. Regional coronary endothelial function is closely related to local early coronary atherosclerosis in patients with mild coronary artery disease: pilot study. *Circ Cardiovasc Imaging* 2012;5:341–348.
17. Kelle S, Hays AG, Hirsch GA, et al. Coronary artery distensibility assessed by 3.0 Tesla coronary magnetic resonance imaging in subjects with and without coronary artery disease. *Am J Cardiol* 2011; 108:491–497.
18. Hays AG, Stuber M, Hirsch GA, Yu J, Schar M, Weiss RG, Gerstenblith G, Kelle S. Non-invasive detection of coronary endothelial response to sequential handgrip exercise in coronary artery disease patients and healthy adults. *PloS One* 2013;8:e58047.
19. Dodge JT Jr, Brown BG, Bolson EL, Dodge HT. Lumen diameter of normal human coronary arteries. Influence of age, sex, anatomic variation, and left ventricular hypertrophy or dilation. *Circulation* 1992; 86:232–246.
20. Yerly J, Ginami G, Nordio G, Coristine AJ, Coppo S, Monney P, Stuber M. Coronary endothelial function assessment using self-gated cardiac cine MRI and k-t sparse SENSE. *Magn Reson Med* 2016;76: 1443–1454.
21. Huber ME, Stuber M, Botnar RM, Boesiger P, Manning WJ. Low-cost MR-compatible moving heart phantom. *J Cardiovasc Magn Reson* 2000;2:181–187.
22. Hays AG, Iantorno M, Soleimanifard S, Steinberg A, Schar M, Gerstenblith G, Stuber M, Weiss RG. Coronary vasomotor responses to isometric handgrip exercise are primarily mediated by nitric oxide: a noninvasive MRI test of coronary endothelial function. *Am J Physiol Heart Circ Physiol*. 2015;308:H1343–H1350.
23. Lusted LB. Decision-making studies in patient management. *N Engl J Med* 1971;284:416–424.
24. Brown CD, Davis HT. Receiver operating characteristics curves and related decision measures: a tutorial. *Chemometr Intell Lab Syst* 2006;80:24–38.
25. Hanley JA, McNeil BJ. The meaning and use of the area under a receiver operating characteristic (ROC) curve. *Radiology* 1982;143:29–36.
26. Park SH, Goo JM, Jo CH. Receiver operating characteristic (ROC) curve: practical review for radiologists. *Korean J Radiol* 2004;5:11–18.
27. Gao YR, Drew PJ. Determination of vessel cross-sectional area by thresholding in Radon space. *J Cereb Blood Flow Metab* 2014;34: 1180–1187.
28. MacAlpin RN, Abbasi AS, Grollman JH Jr, Eber L. Human coronary artery size during life. A cinearteriographic study. *Radiology* 1973; 108:567–576.
29. Terashima M, Meyer CH, Keeffe BG, Putz EJ, de la Pena-Almuguer E, Yang PC, Hu BS, Nishimura DG, McConnell MV. Noninvasive assessment of coronary vasodilation using magnetic resonance angiography. *J Am Coll Cardiol* 2005;45:104–110.
30. Coppo S, Firsova M, Locca D, Knebel JF, van Heeswijk RB, Stuber M. Repositioning precision of coronary arteries measured on X-ray angiography and its implications for coronary MR angiography. *J Magn Reson Imaging* 2015;41:1251–1258.
31. Dietrich O, Raya JG, Reeder SB, Reiser MF, Schoenberg SO. Measurement of signal-to-noise ratios in MR images: influence of multichannel coils, parallel imaging, and reconstruction filters. *J Magn Reson Imaging* 2007;26:375–385.
32. Gilbert O. Measurement of signal-to-noise ratios in sum-of-squares MR images. *J Magn Reson Imaging* 2007;26:1678; author reply 1679.

SUPPORTING INFORMATION

Additional supporting information may be found in the online version of this article

Fig. S1. Linear regression analyses of the area measurements under moving conditions for the different spatial resolutions and noise levels investigated in this study.

Fig. S2. Plots of the SNR (a-b), accuracy (c-d) and precision (e-f) results under static (left column) and moving (right column) conditions. Sub-figures show the mean and standard deviation for every noise level n , pixel size p , and moving condition m (ie, static or moving).

Fig. S3. Bar plots showing the results of the analyses of variance. The graphs illustrate the mean and standard error for the SNR (a-b), accuracy (c-d) and precision (e-f) results. The left column compares the means between the static and moving conditions. The right column compares the means between the five different spatial resolutions. The asterisks indicate significance at different levels: * $P < 0.05$, ** $P < 0.001$.